Highly-dispersed nickel nanoparticles decorated titanium dioxide nanotube array for enhanced solar light absorption

Jian Chen[a] , Yingke Zhou[a,*], Ruizhi Li[a] , Xi Wang[a], George Z. Chen[a,b,*]

[a]The State Key Laboratory of Refractories and Metallurgy, Institute of Advanced Materials and Nanotechnology, College of Materials and Metallurgy, Wuhan University of Science and Technology, Wuhan 430081, P. R. China.

E-mail: zhouyk888@hotmail.com.

[b]Energy Engineering Research Group, Faculty of Science and Engineering, University of Nottingham Ningbo China, Ningbo 316100, P. R. China.

E-mail: george.chen@nottingham.ac.uk.

Abstract

Honeycomb titanium dioxide nanotube array (TiO_2-NTA) decorated by highly-dispersed nickel nanoparticles (Ni-NPs) has been grown under control on Ti foil by anodization and subsequent electrodeposition. The pore diameter and length of TiO_2-NTA, and the size and quantity of Ni-NPs can be controlled via modulating the variables of the electrochemical processes. It has been found that the pretreatment of TiO_2-NTA in the $Cu(NO_3)_2$ solution and further annealing at 450 °C in air could greatly improve the dispersion of the electrodeposited Ni-NPs. Absorption of the light in the solar spectrum from 300 to 2500 nm by the Ni-NPs@TiO_2-NTA is as high as 96.83%, thanks to the co-effect of the light-trapping of TiO_2-NTA and the plasmonic resonance of Ni-NPs. In the water heating experiment performed under an illuminating solar power density of ~1 kWm^{-2} (AM 1.5), the ultimate temperature over 66 °C and an overall efficiency of 78.9% within 30 min were obtained, promising for applications in photothermal conversion and solar energy harvest.

Keywords: titanium dioxide nanotube array; nickel nanoparticles; plasmonic resonance; light absorption; photothermal conversion

1. Introduction

Photo-thermal conversion, the direct way of solar utilization, is one of the key methods to harvest solar energy and has been widely studied in, for example, water steam generation [1-5], desalination [6-8], solar thermal power generation [9, 10], solar thermoelectric conversion [11, 12], and solar fuel production [13]. A highly efficient absorber is the crucial part of a solar collection system, which absorbs solar energy, converts it directly to thermal energy which is then absorbed by a heat transfer fluid. As of now, there are three types of mainstream photothermal conversion materials that have been proposed and studied, including the carbon-based materials, metallic plasmonic materials and semiconducting materials [14, 15, 16].

Up to now, various metal nanoparticles (e.g., Au-NPs [15], Ag-NPs [17], Al-NPs [6, 18] and In-NPs [7]) have been found excellent for light absorption and photothermal conversion based on the surface plasmonic resonance, a collective oscillation of free electrons in the metal stimulated by photons with the matching frequency [19]. Nevertheless, there are some barriers to large-scale applications. For instance, Au and Ag are noble metals, leading to a high cost, whilst Al-NPs and In-NPs with relatively chemical activity are usually prepared by a complex process, including vacuum deposition. In Ni-NPs, the transitions of sp-electrons and partially filled d-bands ($3d^8$) contribute to enhanced absorption in a broader spectral region [20-22], which is desired for harvesting solar energy [23, 24]. Although their light absorption capability is weaker than noble metal nanoparticles, Ni-NPs are a promising alternative for light absorption due to their low-cost as well as feasible and facile synthesis by various methods,

including chemical reduction and electrodeposition [25, 26].

TiO_2, a widely studied semiconductor with a wide band gap of ~3.2 eV, only responds to the ultraviolet (7% of total spectrum) and is usually served as the matrix or support in absorbing materials owing to the good stability, such as C-TiO_2 [27], CNT-TiO_2 [28] and Au-TiO_2 [29], where various rough or porous surface structures are designed to improve absorption by suppressing the surface reflection. Recently, micro/nano-porous structures with strong light absorption have been designed for solar harvesting due to the improved light-trapping effect of the geometrical interspace, where light goes through multiple reflections and scattering internally, and is absorbed gradually [30-32]. For example, an ultra-low reflectance of 0.045% was achieved on vertical carbon nanotube arrays. Besides, a series of raised micro-nano structures have been in situ fabricated by laser writing on Si [33], copper [34], titanium and tungsten surfaces [35], which all exhibit reflectance below 2.5%. For instance, a recent study demonstrated that the wedge-shaped TiO_2 array could absorb light in the whole solar spectrum [36].

Herein, we report the fabrication of the honeycomb-shaped TiO_2-NTA decorated with Ni-NPs on Ti foil by anodization and subsequent electrodeposition. The porous TiO_2-NTA not only provide the structure for light-trapping but also function as the support for 3-D distributed plasmonic Ni-NPs. The fabrication process is illustrated in Fig.1. Interestingly, Ni-NPs have been found to uniformly deposit on the TiO_2-NTA, and the optimized Ni-NPs@TiO_2-NTA hybrid exhibits a strong absorption in the solar spectrum of 0.3~2.5 μm, confirming the potential application of this unique hybrid for

harvesting solar energy.

2. Experimental Section

2.1 Preparation of TiO_2-NTA

Ti sheets (99.5% purity) were cut into desired sizes (e.g. 50×33×0.2 mm^3), polished from coarse to fine on sand papers, ultrasonically cleaned in ethanol and dried in air. Adhesive tapes were to used cover the back of the Ti sheet so that only one side of the sheet with an area of 10 cm^2 was exposed to the electrolyte. Highly uniform and ordered amorphous TiO_2-NTA (a-TiO_2-NTA) were fabricated by a two-step anodization process [37]. All the anodization experiments were carried out at 25 °C in a conventional two-electrode cell with graphite as the cathode. The first-step was performed at 20, 40, 60, 80 V for 0.5 hr in the ethylene glycol electrolyte containing 0.7 wt% NH_4F, 6 vol% H_2O and 4 vol% H_3PO_4. The first-anodized a-TiO_2-NTA were washed in deionized water and the anodized film was taken off using an adhesive tape to expose the pre-patterned Ti substrate. The second-step anodization was performed in the identical electrolyte for 10~70 min, and the voltage was usually 20 V higher than the corresponding first-step. The samples were then washed in ethanol to remove the residual electrolyte and the adhesive tape was removed from the back of the anodized Ti sheet. Subsequently, the anodized Ti sheets were soaked into a 0.05 M $Cu(NO_3)_2 \cdot 3H_2O$ ethanol solution for 6 hr and annealed in air at 450 °C for 3 hr.

2.2 Preparation of Ni-NPs@TiO_2-NTA

The Ni-NPs were deposited on the wall and surface of the TiO_2-NTA by electrodeposition under a constant current in a two-electrode cell containing 0.3 M

$NiSO_4 \cdot 7H_2O$, 0.3 M H_3BO_3 and 0.1 g L^{-1} lauryl sodium sulfate. In this cell, the cathode was the annealed Ti sheet, and the anode was graphite. The electrodeposition was carried out at 35 °C under a high current density of 30 mA cm^{-1} for 0~100 s. Finally, the obtained black samples were washed in water, and dried at 80 °C in air.

2.3. Characterization of materials

The morphology of Ni-NPs@TiO_2-NTA on the Ti substrate was characterized with a scanning electron microscope (SEM, PHILPS XL30TMP). The phase compositions of the samples were recorded by an X-ray diffractometer (XRD, Xpert Pro MPD). The superficial elementary composition and chemical state were characterized by the X-ray photoelectron spectroscopy (XPS, ESCALAB 250Xi). Optical properties (reflectance and absorptance) and band gap were measured by a UV-Vis and NIR spectrophotometer (Shimadzu 3600 UV/Vis and Shimadzu 2600 UV/Vis) incorporated with an integrating sphere. The overall thermal efficiencies of samples were investigated using an in-house designed water heating cell under the radiation (AM 1.5) of a solar simulator (LSP-X500A). The simulated sunlight irradiated on the Ni-NPs@TiO_2-NTA side of the Ti sheet whose back side formed a part of the wall of the water heating cell containing 8.5 mL water.

3. Results and discussion

3.1 Morphologies and structures

The digital photographs shown in Fig.2 were taken from the surfaces of the Ti sheet at the end of each step of polishing and cleaning (Fig. 2a), removing the first-anodized film (Fig. 2b), soaking and annealing (Fig. 2c), and depositing Ni-NPs (Fig. 2d). As

shown in Fig. 2b-2d, the gradual darkening of the sample indicates that light absorption would be enhanced seriatim. Typical SEM images of various samples are displayed in Fig. 2e-2h. The pre-patterned Ti substrate after using adhesive tape to remove the first-anodized film was shown in Fig. 2e. The uniform TiO_2 NTA samples with an assemble of unit cells with diameter of 150~200 nm were constructed after the two-step anodization (Fig. 2f). After annealing and constant current depositing, the sparse Ni-NPs with an average diameter of ~65 nm were deposited on the inner wall of each TiO_2-NTA (Fig. 2g). However, when the TiO_2 NTAs were soaked in the dilute $Cu(NO_3)_2$ solution before annealing, the densely packed Ni-NPs with clear contour profiles and decreased average diameter of ~40 nm were uniformly deposited on both the top and wall of each TiO_2-NTA (Fig. 2h).

Furthermore, compared to the reported works [38, 39], the as-prepared Ni-NPs are smaller in size and highly distributed on each TiO_2-NTA, which indicates that the soaking treatment played a key role in the formation of Ni-NPs. Moreover, we observed that when electrodeposition was carried out directly of the annealed Ti sheet without the TiO_2-NTA coating, the deposited Ni formed a continuous, smooth, and dense silvery coating. This change is markedly different from the granular and black Ni-NPs on the TiO_2-NTA. The cause may be that the higher resistance of the TiO_2-NTA reduced the growth rate and the final size of Ni-NPs [40], and the porous TiO_2-NTA offered more 3-D deposition sites for Ni-NPs to hinder the reunion of Ni-NPs [41].

The morphological features of Ni-NPs@TiO_2-NTA, such as pore size, thickness (or the length of the nanotubes) and particle size and amount of Ni-NPs, are the

determinants for light absorption, which were investigated by finely controlling the electrochemical parameters. The diagram shown in Fig. 3a manifests that the pore size of TiO_2-NTA increases with the anodization voltage due to the enhanced electric field [42]. As shown in Fig. 3b, the thickness of TiO_2-NTA also increases with the anodization time, but the growth speed is slowing down. In Fig. 3c-3h, the average particle sizes of Ni-NPs with different deposition times are about 20, 30, 40, 60, 100 and 150 nm, respectively. It is obvious that the particle size and amount of Ni-NPs increase continuously as deposition time increases. As a result, the remaining pore size gradually shrinks and disappears eventually.

The XRD patterns of as-prepared and heat treated Ni-NPs@TiO_2-NTAs are shown in Fig. 4a. The main ingredients of the sample dried at 80 °C are confirmed to be anatase-TiO_2 by the diffraction peaks at 25.3°，37.8°, 48.0°, 53.9° and 55.0° (JCPDF No. 21-1272), metallic Ni at 44.5° and 76.4° (JCPDF No. 04-8050). The diffraction peaks at 35.1°，38.4°, 40.2°, 53.0°, 62.9°and 70.6° belong to the substrate Ti (JCPDF No. 44-1294). There were no visible diffraction peaks of NiO in the XRD patterns if the sample was heated at temperatures lower than 250 °C, indicating that the metallic Ni is stable in air below 250 °C. When the temperature rose to 300 °C and 350 °C, the apparent diffraction peak at 43.2° for NiO (JCPDF No. 47-1049), as well as the enlarged diameter Ni-NPs shown in Fig.4b indicate that the Ni-NPs were oxidized and transformed to NiO. In later experiments, the Ni-NPs@TiO_2-NTA were heated at 500 °C for 5 h in a reducing atmosphere containing 5% hydrogen. As shown in Fig.4c, in the reducing atmosphere, the Ni-NPs deposited on side wall of TiO_2-NTA grew up

due to the combination of smaller particles at high temperatures, whilst the Ni-NPs deposited on top of TiO_2-NTA were still spherical.

3.2 Light absorption

The light absorption abilities of the Ni-NPs@TiO_2-NTA samples were measured via spectrophotometers with an integrating sphere and evaluated by absorptance and reflectance. The weighted solar absorptance (α) was calculated according to the measured reflection spectrum and standard solar radiation spectrum by the following equations [43]:

$$\alpha = \frac{\int_{0.3\ \mu m}^{2.5\ \mu m}(1-R(\lambda))I_{sol}(\lambda)d\lambda}{\int_{0.3\ \mu m}^{2.5\ \mu m} I_{sol}(\lambda)d\lambda} \quad (1)$$

where λ is the wavelength, $R(\lambda)$ is the reflectance of per unit wavelength for the fabricated samples. I_{sol} (λ) is the solar radiation intensity of per unit wavelength, accroding to the ISO standard 9845-1(1992) of AM 1.5. The band gap (or energy gap) of the different TiO_2 samples was calculated by the Kubelka-Munk equation of $F(R)=(1-R)^2/(2R)$, where R is the reflectance relative to $BaSO_4$ [44].

As shown in Fig. 5a, the polished Ti sheet showed the highest reflectance because of the well-polished surface and intrinsic low absorption of metallic Ti. Compared to the compact TiO_2 film on annealed Ti, the absorptance of TiO_2-NTA further increased as the porous surface captured more light. The lowest reflectance was observed on the Ni-NPs@TiO_2-NTA sample due to the intensive additional absorption of Ni-NPs based on plasma resonance, which is a well-known effect of metal nanoparticles. Although it has been reported that CuO nanoparticles also exhibit the absorption, scattering and plasmon effect in the solar spectrum [45], the low content (~0.56 at% Cu from EDS but

invisible in SEM images) and the cover of Ni-NPs may lead to little absorption via CuO itself. As shown in Fig. 5b, the absorption cutoff wavelength (λ_1 and λ_2) of the TiO_2-NTA without and with soaking is respectively ~390 nm and 415 nm, and the TiO_2-NTA with soaking exhibits stronger absorption in the visible light region, but weaker in the ultraviolet region. The possible reason is that the CuO with a narrow band gap of ~1.7 eV has a strong absorption capacity in the visible region and may decrease the absorption of the TiO_2-NTA in the ultraviolet region due to the shielding effect. The Kubelka–Munk plots in the insert of Fig. 5b demonstrate the band gaps of 3.11 and 2.90 eV of the unsoaked and soaked samples, and the reduced bandgap of the latter may be originated from the Cu^{2+} doping of the substrate [46]. Compared to the unsoaked sample, the absorption of the Ni-deposited TiO_2-NTA with soaking is increased by ~5% (Fig. 5c), and the amount of the Ni-NPs is increased and the size is decreased (Fig. 2g and 2h), indicating that a small quantity of CuO resulted from the decomposion of the absorbed $Cu(NO_3)_2$ may enhance the absorption of Ni-NPs@TiO_2-NTA by modulating the nucleation and changing the morphology of the Ni-NPs [47]. Furthermore, the competitive growth of between different Ni-NPs may restrain themselves to grow larger within the microscopic space of the TiO_2 nanotubes where electrolyte and Ni^{2+} supply was limited. As a result, the Ni-NPs with smaller size (~40 nm) and well distributed on the TiO_2-NTA, exhibited stronger light absorption in the band of 300~1200 nm, but a lower absorption in the middle to far infrared regions, which can be ascribed to the size-dependent resonance theory that the most intense absorption region of plasmonic metal particles depends on their size and shape, and the absorption band red shifts with the

increase of particle size and aspect ratio [48-51]. By the way, absorption region varies with the size of Ni-NPs, therefore the very many Ni-NPs with varying sizes could exhibit a broad light absorption region. Fig.5d shows the reflection spectra for the Ni-NPs@TiO_2-NTA with different pore sizes. It can be seen that the absorption region and overall absorptance are approximately equal, indicating that the absorption for Ni-NPs@TiO_2-NTA is not sensitive to the pore size. Although a larger TiO_2 nanotube can accommodate more Ni-NPs and capture more light for a single nanotube, the whole surface area and amount of loaded Ni-NPs are inversely proportional to the diameter of the pore. Therefore, the Ni-NPs@TiO_2-NTA anodized at 60 V with the appropriate pore size of ~145 nm showed the highest absorptance.

The influence of the Ni-NPs@TiO_2-NTA thickness on light absorption is demonstrated in Fig. 6a. Firstly, distinct fluctuations can be seen in the reflection spectra for Ni-NPs@TiO_2-NTA with thickness of 0.5 and 1.0 μm, which can be ascribed to the destructive and constructive interferences [52, 53]. Also, the overall absorptance increases with the thickness due to more thorough absorption in the longer optical path. Specifically, as the coatings became thicker, more Ni-NPs were deposited on the inner walls and more reflection and scattering occurred in the tubes, contributing to higher absorptance. Although the absorptance of the 2.5 μm thick coating was up to 97.24%, the coating would crimp and detach from the Ti substrate easily, likely because growth in thick Ni-NPs@TiO_2-NTA was likely uneven, and hence cause localized stress development. Therefore, an optimal thickness of 2 μm was set in the subsequent experiments.

As shown in Fig. 6b, the reflection spectra are shown for a series of Ni-NPs@TiO_2-NTA anodized at 60 V for 50 min followed by electrodeposition at various times. With the extension of deposition time (less than 25 s), the amount and size of Ni-NPs increased gradually, due to the adequate nucleation and growth of the particles. The whole band absorptance increased with the increase of the number of Ni-NPs. The Ni-NPs@TiO_2-NTA obtained from deposition for 25 s displayed the highest absorptance of visible light and a maximum whole spectrum absorptance of 96.83%, which is comparative to that of the reported materials with similar porous structures, such as the Al-NPs@Al_2O_3-NTA (~96%), Au@Al_2O_3 (91%) and the Ni particles pigmented anodized aluminum (94-96%) [4, 29, 54]. However, when the deposition time was further prolonged (more than 25 s), the deposited Ni-NPs grew big enough to fill the pores. The pore size gradually decreased with the continuous deposition of Ni particles, and more light was reflected off the surface, rather than enter the nanotubes, leading to the deterioration of absorptance especially for the visible light (the color of the sample converted to yellow and white).

The Ni-NPs@TiO_2-NTA samples were further thermally treated at different temperatures and atmospheres. As shown in Fig. 6c, the absorptance did not decline when the temperature was lower than 250 ^oC, but significantly deteriorated at 300 ^oC, indicating that the metallic Ni-NPs with high light absorption could remain stable at 250 ^oC, but the nickel oxides formed at higher temperatures behaved poorly in light absorption. On the other hand, the substances such as black nickel compounds of

NiOOH and Ni_2O_3 may both exist in the Ni-NPs@TiO_2-NTA and contribute to light absorption. In later experiments, the Ni-NPs@TiO_2-NTA were heated at 500 ^oC in the reducing atmosphere containing 5% hydrogen. Consequently, the reflectance as shown in Fig. 6d attenuated slightly in the visible region and a little enhancement in the infrared region, probably due to the growth, fusion and aggregation of Ni-NPs at 500 ^oC. In summary, the high and deteriorated absorptances of Ni-NPs@TiO_2-NTA without and with thermal oxidation indicate that the metallic Ni-NPs with sufficient number of free electrons are crucial to the high absorptance.

3.3 Photothermal conversion

To directly observe the photothermal conversion properties of Ni-NPs@TiO_2-NTA, water heating experiments (shown as Fig.7a and 7b) were performed. The samples were combined into plastic boxes with a volume of 3×3×1 cm^3, in which 8.5 mL water with an initial temperature of 20.5±0.2 ^oC was filled up and a thermometer was inserted to monitor the temperature. In addition, the plastic boxes were thermally insulated by closed-cell foam to reduce heat loss. The light was provided by a solar simulator with standard radiation intensity of AM 1.5. The sample was irradiated vertically for 60 min, and the temperature variation was recorded every minute. As the thickness of Ni-NPs@TiO_2-NTA is far less than that of the Ti sheet (~200 μm), all samples are approximately identical in thickness and thermal conductivity. Therefore, the heat generated at the top surface conducts to the Ti substrate and then to the water whose temperature can be detected to evaluate the average thermal efficiency (ATE). The ATE can be calculated by equation (2) [55],

$$\eta = \frac{C \times m \times \Delta T}{I \times S \times t} \quad (2)$$

where C is the specific heat capacity of water which is approximately 4200 J $kg^{-1}K^{-1}$, m the mass of water (ca. 8.5 g), ΔT the temperature rise, I the power density of the light source (1 kW m^{-2}), S the irradiated area of the sample (10 cm^2), and t the time for irradiation. Consider that the heating rates of all the samples decreased gradually and reached at the equilibrium temperature within 57 min, we calculated the overall PTEC of irradiation for 30 min and 57 min, respectively. Obviously, the ATE for 30 min was higher than that for 57 min because the thermal loss, particularly infrared radiation and conduction, also increased with the temperature.

In Fig. 7c and 7e, it is obvious that the polished Ti sheet demonstrated the lowest heating rate and ATE due to its high reflectance (>40%). As the thickness of the Ni-NPs@TiO_2-NTA increased, the heating rate and the equilibrium temperature also increased, and the 2 μm thick Ni-NPs@TiO_2-NTA showed the fastest heating and the highest equilibrium temperature (66.5 ^oC) and ATE (78.9% for 30 min and 48.0% for 57 min), which can be positively correlated with the absorptance. In Fig. 7d and 7f, the heating rate, the equilibrium temperature and the overall PTCE are also positively correlated with the absorptance, and the 2 μm thick Ni-NPs@TiO_2-NTA obtained by 25 s deposition showed the highest ATE.

4. Conclusions

The Ni-NPs@TiO_2-NTA have been synthesized on the Ti substrate by anodization and electrodeposition. A pretreatment of the TiO_2-NTA in the ethanol solution of $Cu(NO_3)_2$ can significantly downsize the Ni-NPs and enhance light absorption by about

5%. The absorptance increases with the thickness of the Ni-NPs@TiO_2-NTA, but is not sensitive to the pore size. Moreover, the size and amount of Ni-NPs have a significant influence on light absorption. Thanks to the light-trapping ability of the porous TiO_2-NTA and the surface plasmon resonance of Ni-NPs, a high absorptance of 96.83% in the solar spectrum from 300 to 2500 nm has been achieved. In the water heating experiment, the highest temperature over 66 ^oC and an overall efficiency of 78.9% within 30 min irradiation have been obtained, implying the potential applications of the Ni-NPs@TiO_2-NTA in light-to-heat conversion and solar energy harvest.

Acknowledgements

This work was supported by the National Natural Science Foundation of China (No. 51372178) and the Natural Science Foundation of Hubei Province of China (No. 2013CFA021, 2018CFA022).

Reference

[1] G. Ni, G. Li, S.V. Boriskina, H. Li, W. Yang, T. Zhang, G. Chen, Steam generation under one sun enabled by a floating structure with thermal concentration, Nat. Energy 1 (2016) 16126.

[2] K. Bae, G. Kang, S.K. Cho, W. Park, K. Kim, W.J. Padilla, Flexible thin-film black gold membranes with ultrabroadband plasmonic nanofocusing for efficient solar vapour generation, Nature Commu. 6 (2015) 10103.

[3] H.L. Ren, M. Tang, B.L. Guan, K.X. Wang, J.W. Yang, F.F. Wang, M.Z. Wang, J.Y. Shan, Z.L. Chen, D. Wei, H.L. Peng and Z.F. Liu, Hierarchical Graphene Foam for Efficient Omnidirectional Solar-Thermal Energy Conversion, Adv. Mater. 29 (2017) 1702590.

[4] L. Zhou, Y.L. Tan, D.X. Ji, B. Zhu, P. Zhang, J. Xu, Q.Q. Gan, Z.F. Yu and J. Zhu, Self-assembly of highly efficient, broadband plasmonic absorbers for solar steam generation, Sci. Adv. 2 (2016) 1501227.

[5] C.J. Chen, Y.J. Li, J.W. Song, Z. Yang, Y.D. Kuang, E. Hitz, C. Jia, A. Gong, F. Jiang, J.Y. Zhu, B. Yang, J. Xie and L.B. Hu, Highly Flexible and Efficient Solar Steam Generation Device, Adv. Mater. 29 (2017) 1701756.

[6] L. Zhou, Y. Tan, J. Wang, W. Xu, Y. Yuan, W. Cai, S. Zhu, J. Zhu, 3D self-assembly of aluminium nanoparticles for plasmon-enhanced solar desalination, Nat. Photo. 10 (2016) 393-398.

[7] L.L. Zhang, J. Xing, X.L. Wen, J.W. Chai, S.J. Wang, Q.H. Xiong, Plasmonic Heating from Indium Nanoparticles on a Floating Microporous Membrane for

Enhanced Solar Seawater Desalination, Nanoscale 9 (2017) 12843-12849.

[8] M.Y. Shang, N. Li, S.D. Zhang, T.T. Zhao, C. Zhang, C. Liu, H.F. Li, Z.Y. Wang, Full-Spectrum Solar-to-Heat Conversion Membrane with Interfacial Plasmonic Heating Ability for High-Efficiency Desalination of Seawater, ACS Appl. Energy Mater. 1 (2017) 56-61.

[9] J.Y. Moon, D.L. Lu, B.V. Saders, T.K. Kim, S.D. Kong, S.H. Jin, R.K. Chen, Z.W. Liu, High performance multi-scaled nanostructured spectrally selective coating for concentrating solar power, Nano Energy 8 (2014) 238-246.

[10] Q.J. Mao, Recent developments in geometrical configurations of thermal energy storage for concentrating solar power plant, Renew. & Sust. Energy Rev. 59 (2016) 320-327.

[11] L.L. Baranowski, G.J. Snyder, E.S. Toberer, Concentrated solar thermoelectric generators, Energy & Environ. Sci. 5 (2012) 9055-9067.

[12] A. Kosuga, Y. Yamamoto, M. Miyai, M. Matsuzawa, Y. Nishimura, S. Hidaka, K. Yamamoto, S. Tanaka, Y. Yamamoto, S. Tokonami, T. Iida, A high performance photothermal film with spherical shell-type metallic nanocomposites for solar thermoelectric conversion, Nanoscale 7 (2015) 7580-7584.

[13] X.G. Meng, T. Wang, L.Q. Liu, S.X. Ouyang, P. Li, H.L. Hu, T. Kako, H. Iwai, A. Tanaka, J.H. Ye, Photothermal conversion of CO_2 into CH_4 with H_2 over Group VIII nanocatalysts: an alternative approach for solar fuel production, Angew. Chemi. 53 (2014) 11662-11666.

[14] J.L.Yang, Y.S. Pang, W.X. Huang, S.K. Shaw, J. Schiffbauer, M.A. Pillers, X. Mu,

S.R. Luo, T. Zhang, Y.J. Huang, G.X. Li, S. Ptasinska, M. Lieberman, T.F. Luo, Functionalized Graphene Enables Highly Efficient Solar Thermal Steam Generation, ACS nano 11 (2017) 5510-5536.

[15] X.Z. Wang, Y.R. He, X. Liu, G. Cheng, J.Q. Zhu, Solar steam generation through bio-inspired interface heating of broadband-absorbing plasmonic membranes, Appl. Energy 195 (2017) 414-425.

[16] M.M. Ye, J. Jia, Z.J. Wu, C.X. Qian, R. Chen, P.G. O'Brien, W. Sun, Y.C. Dong, G.A. Ozin, Synthesis of Black TiO_x Nanoparticles by Mg Reduction of TiO_2 Nanocrystals and their Application for Solar Water Evaporation, Adv. Energy Mater. 7 (2017) 1601811.

[17] F. Wu, X.Y. Hu. J. Fan, E.Z. Liu, T. Sun, L.M. Kang, W.Q. Hou, C.J. Zhu, H.C. Liu, Photocatalytic Activity of Ag/TiO_2 Nanotube Arrays Enhanced by Surface Plasmon Resonance and Application in Hydrogen Evolution by Water Splitting, Plasmonics 8 (2013) 501-508.

[18] D.B. Zhang, X.F. Yang, X.K. Hong, Y.S. Liu, J.F. Feng, Aluminum nanoparticles enhanced light absorption in silicon solar cell by surface plasmon resonance, Opt. Quan. Electr. 47 (2014) 1421-1427.

[19] G. Dodekatos, S. Schunemann, H. Tuysuz, Surface Plasmon-Assisted Solar Energy Conversion, Top. Cur. Chem. 371 (2015) 215-252.

[20] S. Zhu, L.M. Wang, Optical and magnetic properties of Ni nanoparticles in rutile formed by Ni ion implantation, Appl. Phys. Lett. 88 (2006).

[21] V. Dalouji, Effect of deposition time on surface plasmon resonance and Maxwell-

Garnett absorption in RF-magnetron sputtered carbon-nickel films, Mater. Sci. Poland 34 (2016) 337-343.

[22] X. Xiang, X.T. Zu, S. Zhu, L.M. Wang, Optical properties of metallic nanoparticles in Ni-ion-implanted α-Al_2O_3 single crystals, Appl. Phys. Lett. 84 (2004) 52-54.

[23] M. Farooq, A.A. Green. M.G. Hutchins, High performance sputtered Ni : SiO2 composite solar absorber surfaces, Sol. Energy Mater. Sol. Cells 54 (1998) 67-73.

[24] F. Cao, D. Kraemer, T.Y. Sun, Y.C. Lan, G. Chen, Z.F. Ren, Enhanced Thermal Stability of W-Ni-Al_2O_3Cermet-Based Spectrally Selective Solar Absorbers with Tungsten Infrared Reflectors, Adv. Energy Mater. 5 (2015) 1401042.

[25] L.H. Chou, W.C. Hung, M.T. Lee, On the Preparation of Nickel Nanoparticles by Chemical Reduction Method: X-ray Absorption Spectroscopy, Mater. Sci. 22 (2016) 305-308.

[26] Y.H. Zhang, Y.N. Yang, P. Xiao, X.N. Zhang, L. Lu, L. Li, Preparation of Ni nanoparticle-TiO_2 nanotube composite by pulse electrodeposition, Mater. Lett. 63 (2009) 2429-2431.

[27] B. Cheng, K.K. Wang, K.P. Wang, W. Jiang, B.J. Cong, C.L. Song, S.H. Jia, G.R. Han, Y. Liu, Porous carbon-titania nanocomposite films for spectrally solar selective absorbers, Sol. Energy Mater. Sol. Cells 133 (2015) 126-132.

[28] M.E. Rincón, J.D. Molina, M. Sánchez, C. Arancibia, E. García, Optical characterization of tandem absorber/reflector systems based on titanium oxide-carbon coatings, Sol. Energy Mater. Sol. Cells 91 (2007) 1421-1425.

[29] E.Z. Liu, J. Fan, X.Y. Hu, Y. Hu, H. Li, C.N. Tang, L. Sun, J. Wan, A facile strategy

to fabricate plasmonic Au/TiO_2 nano-grass films with overlapping visible light-harvesting structures for H_2 production from water, J. Mater. Sci. 50 (2014) 2298-2305.

[30] Y. Li, Z.Y. Fu, B.L. Su, Hierarchically Structured Porous Materials for Energy Conversion and Storage, Adv. Funct. Mater. 22 (2012) 4634-4667.

[31] S.K. Yang, N. Sun, B.B. Stogin, J. Wang, Y. Huang, T.S. Wong, Ultra-antireflective synthetic brochosomes, Nat. Commu. 8 (2017) 1285-1293.

[32] M. Suzuki, T. Yamamoto, Y. Katayama, S. Kuwata, T. Tanaka, Light Absorption by Metals with Porous Surface Layer Formed by Oxidization and Reduction Treatment, Mater. Trans. 53 (2012) 1556-1562.

[33] J. Yang, F.F. Luo, T.S. Kao, X. Li, G.W. Ho, J.H. Teng, X.G. Luo, M.H. Hong, Design and fabrication of broadband ultralow reflectivity black Si surfaces by laser micro/nanoprocessing, Light: Sci. Appl. 3 (2014) 185.

[34] P.X. Fan, H. Wu, M. L. Zhong, H. J. Zhang, B. F. Bai, G. F. Jin, Large scale cauliflower shaped hierarchical copper nanostructures for efficient photothermal conversion, Nanoscale 8 (2016) 14617-14624.

[35] P.X. Fan, B.F. Bai, M.L. Zhong, H.J. Zhang, J.Y. Long, J.P. Han, W.Q. Wang, G.F. Jin, General Strategy toward Dual-Scale-Controlled Metallic Micro-Nano Hybrid Structures with Ultralow Reflectance, ACS Nano 11 (2017) 7401-7408.

[36] C.L. Liu, W. Zhou, J.K. Song, H.J. Liu, J.H. Qu, L. Guo, G.F. Song, C.P. Huang, Nanostructure-induced colored TiO_2 array photoelectrodes with full solar spectrum harvesting, J. Mater. Chem. A 5 (2017) 3145-3151.

[37] X.M. Zhong, D.L. Yu, Y. Song, D.D. Li, H.P. Xiao, C.Y. Yang, L.F. Lu, W.H. Ma, X.F. Zhu, Fabrication of large diameter TiO_2 nanotubes for improved photoelectrochemical performance, Mater. Res. Bull. 60 (2014) 348-352.

[38] H. Cheshideh, F. Nasirpouri, Cyclic voltammetry deposition of nickel nanoparticles on TiO_2 nanotubes and their enhanced properties for electro-oxidation of methanol, J. Electroanal. Chem. 797 (2017) 121-133.

[39] J.A. Díaz-Real, E.O. Ortega, M.P. Gurrola, J.L. Garcia, L.G. Arriaga, Light-harvesting Ni/TiO_2 nanotubes as photo-electrocatalyst for alcohol oxidation in alkaline media, Electrochim. Acta 206 (2016) 388-399.

[40] J. Lee, J. Yang, S.G. Kwon, T. Hyeon, Nonclassical nucleation and growth of inorganic nanoparticles, Nat. Rev. Mater. 1 (2016) 16034.

[41] P. Li, J. Liu, N. Nag, P.A. Crozier, Dynamic nucleation and growth of Ni nanoparticles on high-surface area titania, Sur. Sci. 600 (2006) 693-702.

[42] J. Ni, K. Noh, C.J. Frandsen, S.D. Kong, G. He, T.T. Tang, S. Jin, Preparation of near micrometer-sized TiO_2 nanotube arrays by high voltage anodization, Mater. Sci. Eng.C 33 (2013) 259-264.

[43] X.H. Gao, Z.M. Guo, Q.F. Geng, P.J. Ma, A.Q. Wang, G. Liu, Microstructure, chromaticity and thermal stability of SS/TiC-WC/Al_2O_3 spectrally selective solar absorbers, Sol. Energy Mater. Sol. Cells 164 (2017) 63-69.

[44] D. Venieri, I. Gounaki, V. Binas, A. Zachopoulos, G. Kiriakidis, D, Mantzavinos, Inactivation of MS_2 coliphage in sewage by solar photocatalysis using metal-doped TiO_2, Appl. Catal. B: Environ. 178 (2014) 54-64.

[45] J. S. Sekhon, S. S. Verma, Cu, CuO, and Cu_2O Nanoparticle Plasmons for Enhanced Scattering in Solar Cells, Renew. Energy and the Environ. OSA Technical Digest (CD) (2011) paper JWE22.

[46] Y.C. Nah, I. Paramasivam, P. Schmuki, Doped TiO_2 and TiO_2 nanotubes: synthesis and applications, Chem. Phys. Chem. 11 (2010) 2698-2713.

[47] S.C.S. Lai, R.A. Lazenby, P.M. Kirkman, P.R. Unwin, Nucleation, aggregative growth and detachment of metal nanoparticles during electrodeposition at electrode surfaces, Chem. Sci. 6 (2015) 1126-1138.

[48] A.K. Guo, Y. Fu, G. Wang, X.B. Wang, Diameter effect of gold nanoparticles on photothermal conversion for solar steam generation, RSC Adv. 7 (2017) 4815-4824.

[49] H.J. Chen, X.S. Kou, Z. Yang, W.H. Ni, J. F. Wang, Shape- and Size-Dependent Refractive Index Sensitivity of Gold Nanoparticles, Langmuir 24 (2008) 5233-5237.

[50] V.N. Pustovit, T.V. Shahbazyan, L.G. Grechko, Size-dependent effects in solutions of small metal nanoparticles, Eur. Phys. J. B 69 (2009) 369-374.

[51] X. Huang, I.H. Elsayed, W. Qian, Cancer cell imaging and photothermal therapy in the near-infrared region by using gold nanorods, J. Am. Che.Soc.128 (2006) 2115-2120.

[52] J.Y. Moon, M. Kemell, R. Punkkinen, H.P. Hedman, B. Park, A. Suominen, L. Heikkilä, H. Kim, A. Tuominen, Interference Colors of TiO_2 Nanotube Arrays Grown by Anodic Oxidation, Adv. Mater. Res. 875-877 (2014) 370-374.

[53] X.L. Zhao, G.W. Meng, Q.L. Xu, F.M. Han, Q. Huang, Color fine-tuning of CNTs@AAO composite thin films via isotropically etching porous AAO before CNT growth and color modification by water infusion, Adv. Mat. 22 (2010) 2637-2641.

[54] P.L. Stefchev, R.P. Kirilov, C.A. Girginov, AC-anodized and Ni-pigmented aluminum for selective solar absorption, Izvestiya Po Khimiya Bulgarska Akademiya Na Naukite 45(2013) 47-51.

[55] K. Jaiganesh, K. Duraiswamy. Experimental study of enhancing the performance of PV panel integrated with solar thermal system, Inter. J. Engin. & Techno. 5(2013) 3419-3426.

Figure captions

Fig. 1. Synthesis procedure for the Ni-NPs@TiO_2-NTA: (a) the original Ti sheet, (b) a-TiO_2-NTA fabricated by a two-step anodizing, (c) the $Cu(NO_3)_2$ solution soaked and annealed TiO_2-NTA, (d) the electrochemically deposited Ni-NPs on TiO_2-NTA, (e) the enlarged part of (d), showing the photothermal conversion mechanisms.

Fig.2. Optical photographs: (a) Ti sheet, (b) Ti sheet after removing the first-anodized film, (c) Annealed TiO_2-NTA, and (d) Ni-NPs@TiO_2-NTA. SEM images: (e) The pre-patterned Ti sheet, (f) TiO_2-NTA, (g) Ni-NPs@TiO_2-NTA without soaking and (h) Ni-NPs@TiO_2-NTA with soaking in the $Cu(NO_3)_2$ solution. The inserts in (f), (g) and (h) are the corresponding enlarged top views.

Fig.3. (a) The average pore size of TiO_2-NTA under different anodization voltages. (b) The average thickness of TiO_2-NTA anodized at 60 V with various anodization times. SEM images of Ni-NPs@TiO_2-NTA with different deposition times: (c) 6.25 s, (d) 12.5 s, (e) 25 s, (f) 50 s, (g) 75 s, (h), 100 s. The TiO_2-NTA in (c) and (h) were anodized at 60 V for 50 min.

Fig.4. (a) XRD patterns of Ni-NPs@TiO_2-NTA treated in air at different temperatures. (b) SEM image of Ni-NPs@TiO_2-NTA treated at 350°C. (c) SEM image of Ni-NPs@TiO_2-NTA treated in H_2/Ar.

Fig.5. (a) Solar radiation spectrum and reflection spectra for different surfaces on Ti substrates. (b) Absorptance spectra and Kubelka–Munk plot (the insert) of TiO_2-NTA with and without soaking. (c) Reflection spectra for Ni-NPs@TiO_2-NTA with and without soaking. (d) Reflection spectra for Ni-NPs@TiO_2-NTA with a thickness of 2 μm and different pore sizes. The data in bracket is the weighted absorptance of the samples.

Fig.6. (a) Reflection spectra for Ni-NPs@TiO_2-NTA with different thicknesses. (b)

Reflection spectra for Ni-NPs@TiO_2-NTA with different Ni deposition times. (c) Reflection spectra for Ni-NPs@TiO_2-NTA with different calcination temperatures. (d) Reflection spectra for Ni-NPs@TiO_2-NTA with H_2 reduction.

Fig.7. (a) Optical photograph of the water heating device. (b) The water heating under illumination and the recorded water temperature. (c) Heating curves of Ni-NPs@TiO_2-NTA with different thicknesses. (d) Heating curve of Ni-NPs@TiO_2-NTA with different deposition times. (e) The ATE of Ni-NPs@TiO_2-NTA in (c), the thickness of Ni-NPs@TiO_2-NTA on pure Ti sheet is regarded as 0. (f) The ATE of Ni-NPs@TiO_2-NTA in (d).

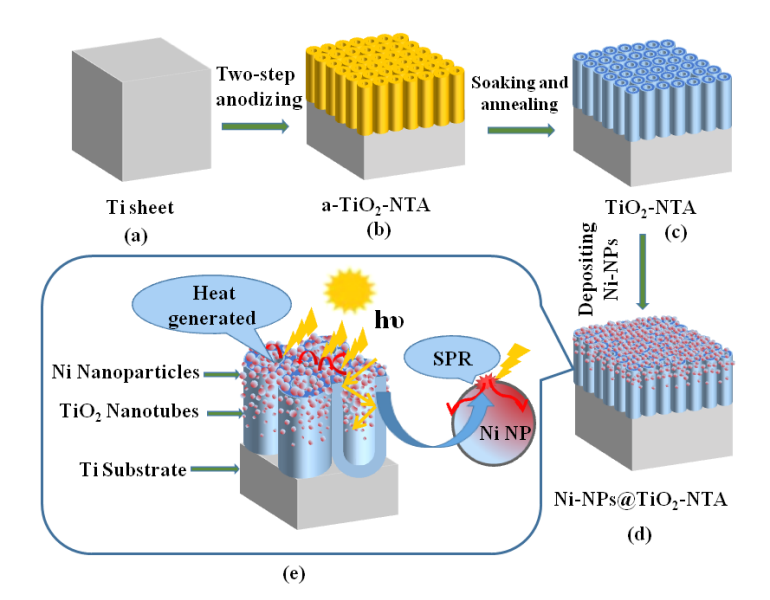
Two-step anodizing
Soaking and annealing
Ti sheet
(a)
a-TiO2-NTA
(b)
TiO2-NTA
(c)
Depositing Ni-NPs
Heat generated
hυ
SPR
Ni Nanoparticles
TiO2 Nanotubes
Ti Substrate
Ni NP
(e)
Ni-NPs@TiO2-NTA
(d)

Fig.1.

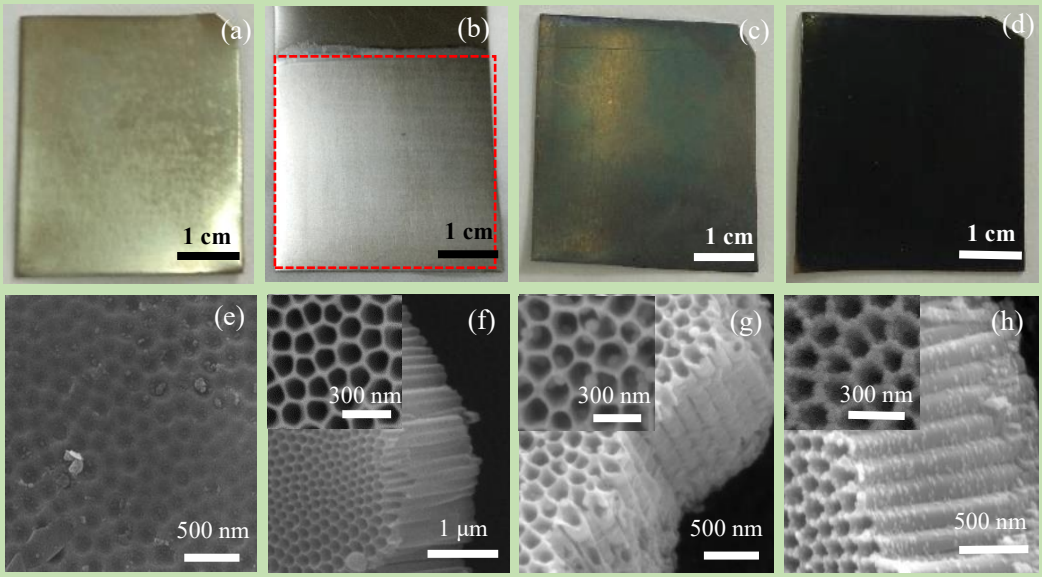
(a)
1 cm
(b)
1 cm
(c)
1 cm
(d)
1 cm
(e)
500 nm
(f)
300 nm
1 μm
(g)
300 nm
500 nm
(h)
300 nm
500 nm

Fig.2.

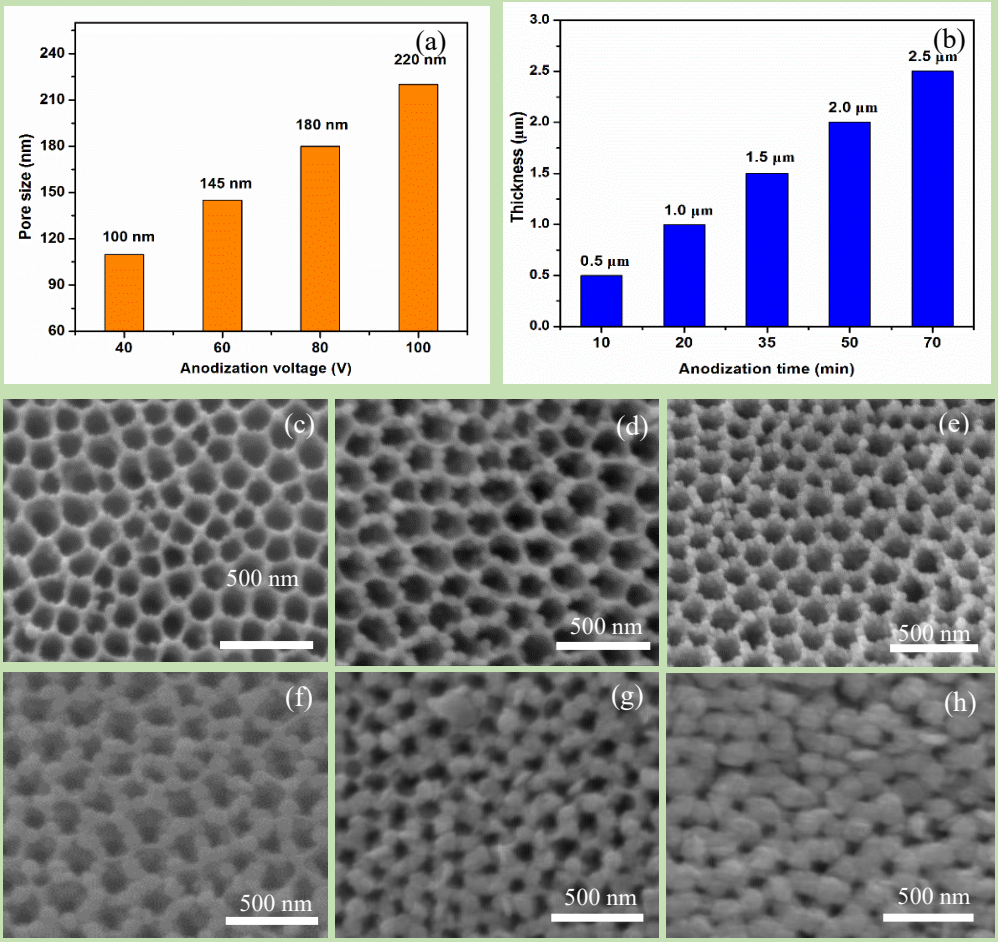
(a)
Pore size (nm)
240
210
180
150
120
90
60
100 nm
145 nm
180 nm
220 nm
40
60
80
100
Anodization voltage (V)
(b)
Thickness (μm)
3.0
2.5
2.0
1.5
1.0
0.5
0.0
0.5 μm
1.0 μm
1.5 μm
2.0 μm
2.5 μm
10
20
35
50
70
Anodization time (min)
(c)
500 nm
(d)
500 nm
(e)
500 nm
(f)
500 nm
(g)
500 nm
(h)
500 nm

Fig.3.

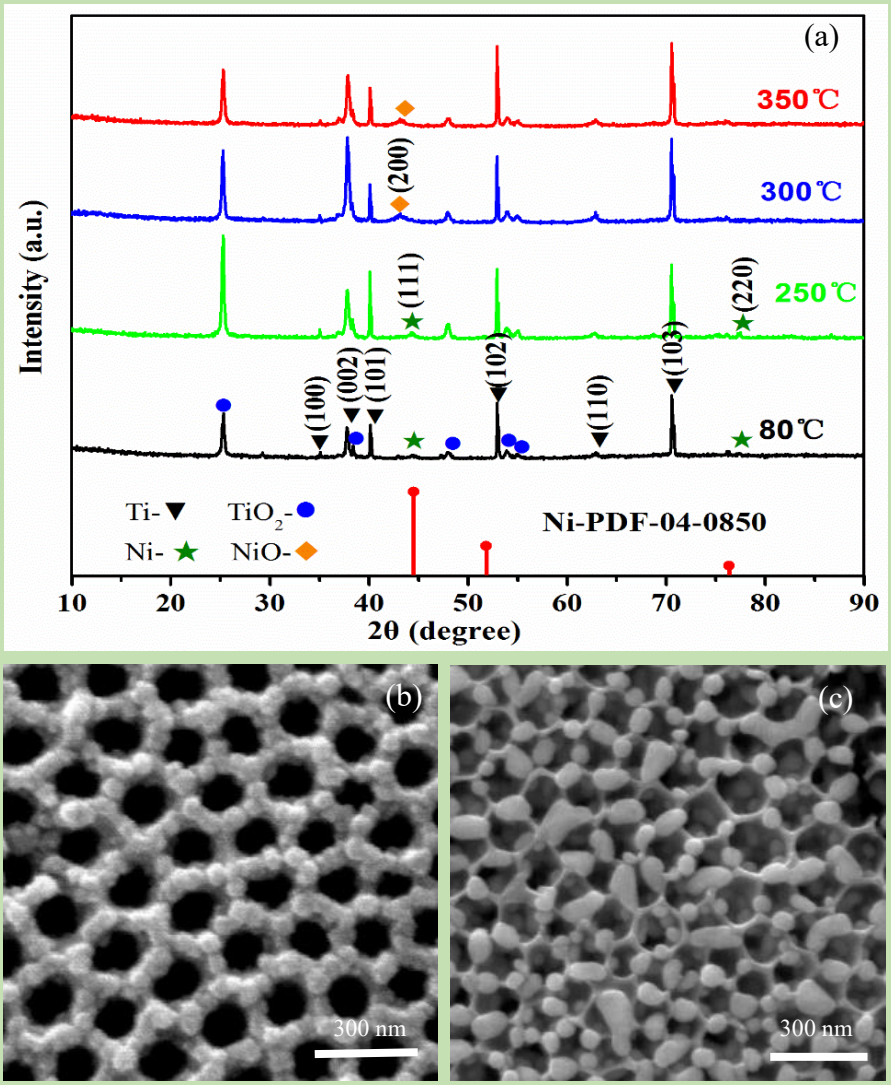
(a)
350℃
300℃
250℃
80℃
(200)
(111)
(220)
(100)
(002)
(101)
(102)
(110)
(103)
Intensity (a.u.)
Ti-▼ TiO2-●
Ni-★ NiO-◆
Ni-PDF-04-0850
10 20 30 40 50 60 70 80 90
2θ (degree)
(b)
300 nm
(c)
300 nm

Fig.4.

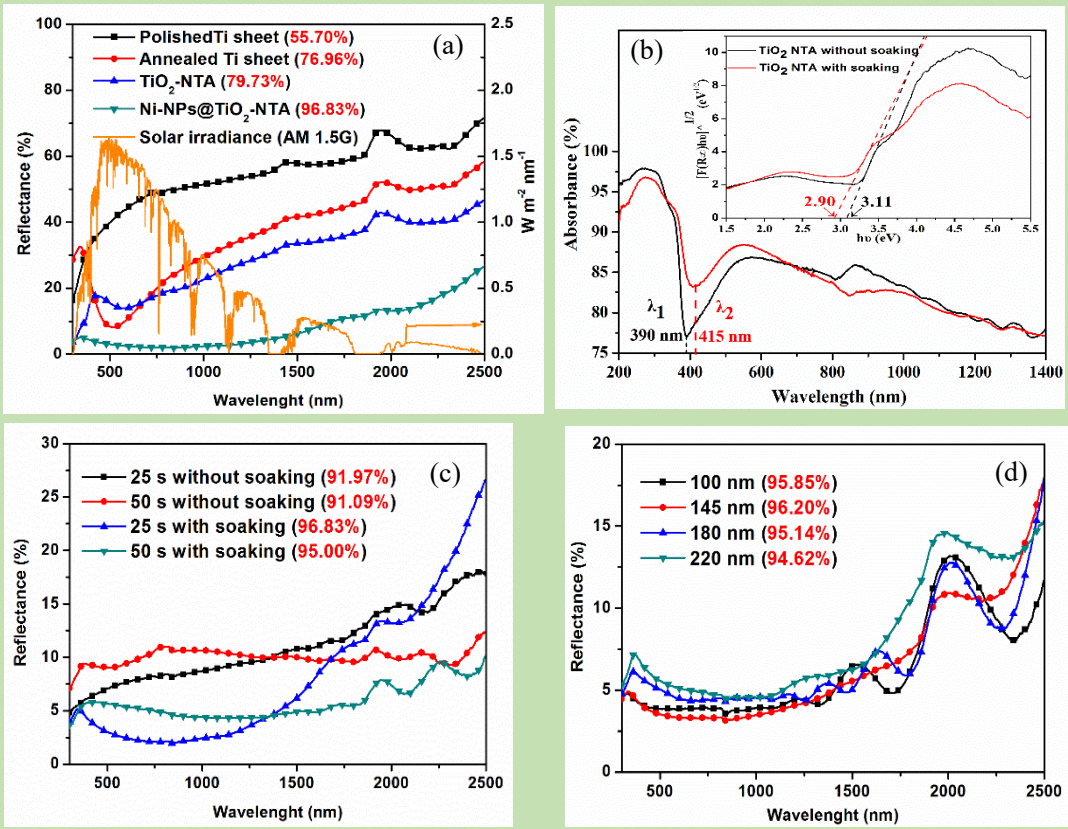
(a)
PolishedTi sheet (55.70%)
Annealed Ti sheet (76.96%)
TiO2-NTA (79.73%)
Ni-NPs@TiO2-NTA (96.83%)
Solar irradiance (AM 1.5G)
Reflectance (%)
W m-2 nm-1
Wavelenght (nm)
(b)
TiO2 NTA without soaking
TiO2 NTA with soaking
2.90
3.11
hυ (eV)
Absorbance (%)
λ1
λ2
390 nm
415 nm
Wavelength (nm)
(c)
25 s without soaking (91.97%)
50 s without soaking (91.09%)
25 s with soaking (96.83%)
50 s with soaking (95.00%)
Reflectance (%)
Wavelenght (nm)
(d)
100 nm (95.85%)
145 nm (96.20%)
180 nm (95.14%)
220 nm (94.62%)
Reflectance (%)
Wavelenght (nm)

Fig.5.

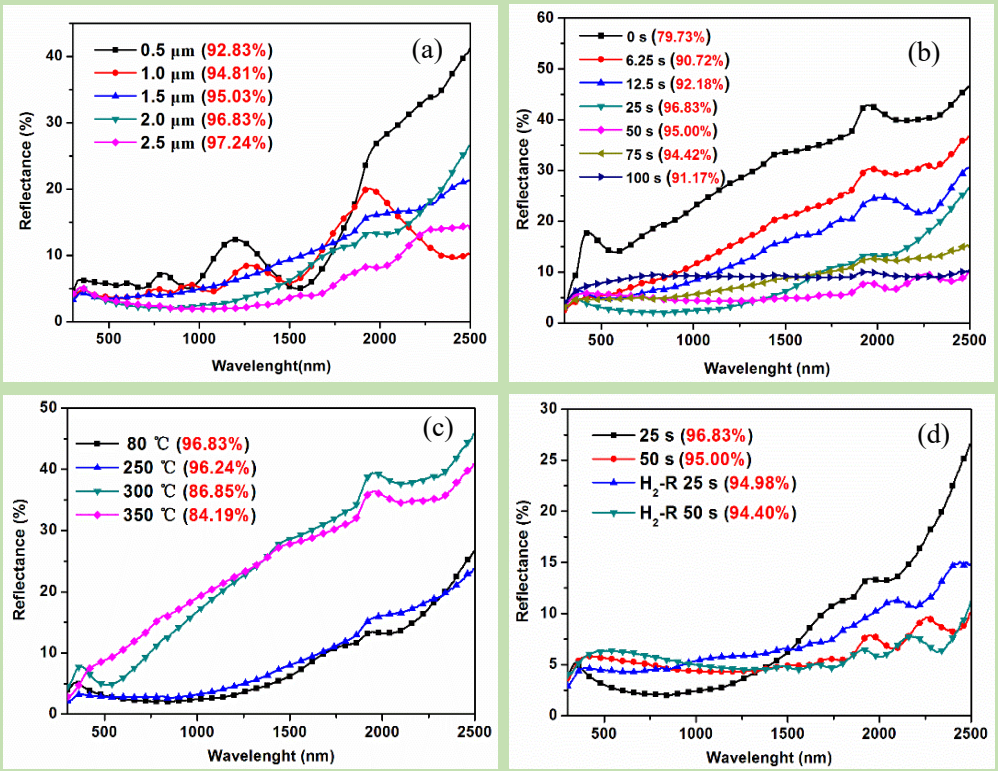
(a)
0.5 μm (92.83%)
1.0 μm (94.81%)
1.5 μm (95.03%)
2.0 μm (96.83%)
2.5 μm (97.24%)
Reflectance (%)
Wavelenght(nm)
(b)
0 s (79.73%)
6.25 s (90.72%)
12.5 s (92.18%)
25 s (96.83%)
50 s (95.00%)
75 s (94.42%)
100 s (91.17%)
Reflectance (%)
Wavelenght (nm)
(c)
80 ℃ (96.83%)
250 ℃ (96.24%)
300 ℃ (86.85%)
350 ℃ (84.19%)
Reflectance (%)
Wavelenght (nm)
(d)
25 s (96.83%)
50 s (95.00%)
H2-R 25 s (94.98%)
H2-R 50 s (94.40%)
Reflectance (%)
Wavelenght (nm)

Fig.6.

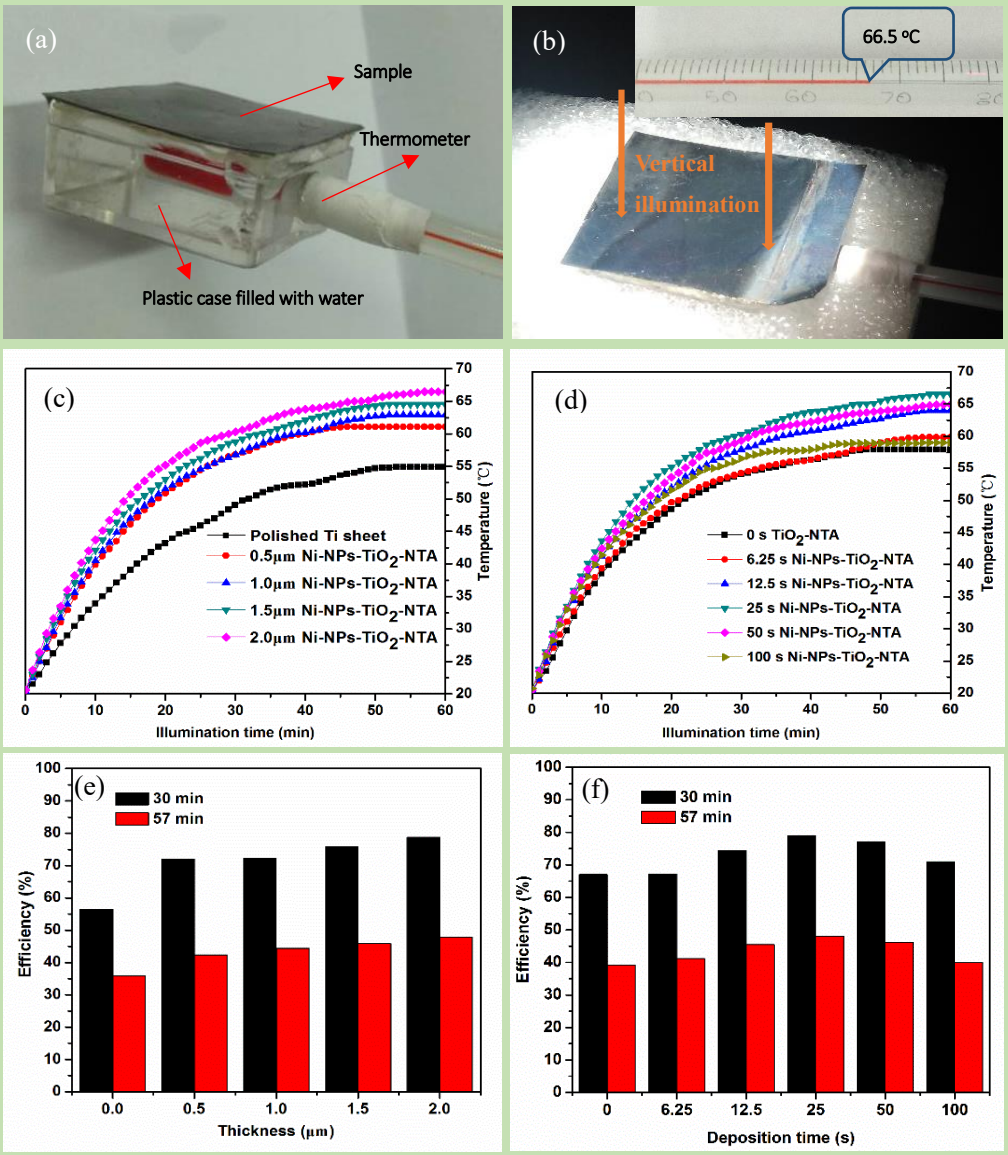
(a)
Sample
Thermometer
Plastic case filled with water
(b)
66.5 °C
Vertical
illumination
(c)
Polished Ti sheet
0.5μm Ni-NPs-TiO2-NTA
1.0μm Ni-NPs-TiO2-NTA
1.5μm Ni-NPs-TiO2-NTA
2.0μm Ni-NPs-TiO2-NTA
Temperature (℃)
Illumination time (min)
(d)
0 s TiO2-NTA
6.25 s Ni-NPs-TiO2-NTA
12.5 s Ni-NPs-TiO2-NTA
25 s Ni-NPs-TiO2-NTA
50 s Ni-NPs-TiO2-NTA
100 s Ni-NPs-TiO2-NTA
Temperature (℃)
Illumination time (min)
(e)
30 min
57 min
Efficiency (%)
Thickness (μm)
(f)
30 min
57 min
Efficiency (%)
Deposition time (s)

Fig.7.

Graphical abstract

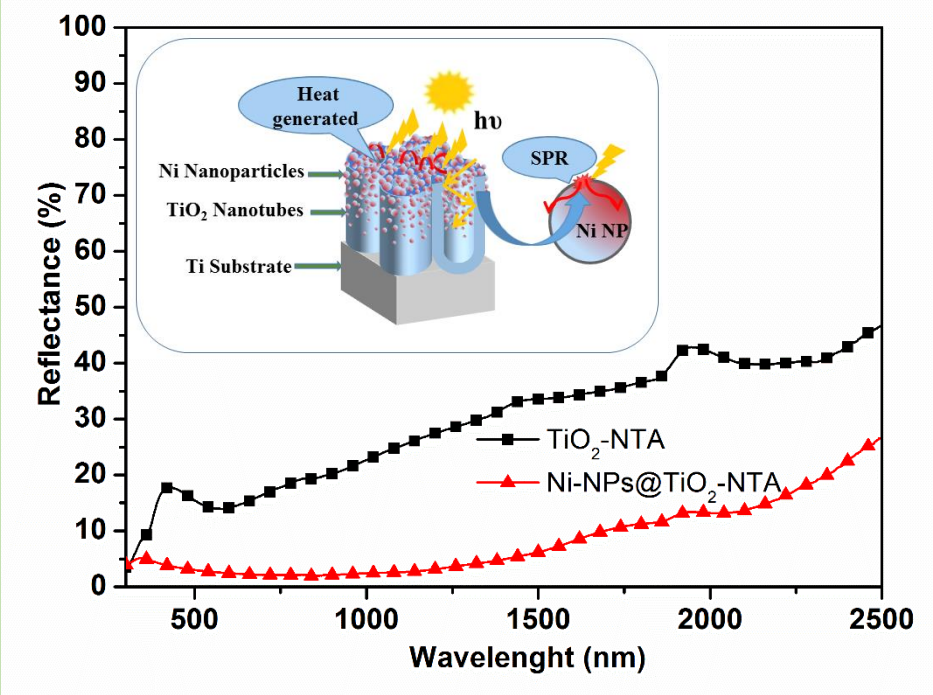

Highlights

- Ni nanoparticles have been highly-dispersed on TiO_2 nanotube array.
- The size of Ni is significantly reduced after the pretreatment of TiO_2.
- The properties of Ni@TiO_2 can be well controlled.
- The composite exhibits high absorption and photothermal conversion efficiency.